High Gas-Phase Methanesulfonic Acid Production in the OH-Initiated Oxidation of Dimethyl Sulfide at Low Temperatures

Jiali Shen, Wiebke Scholz, Xu-Cheng He, Putian Zhou, Guillaume Marie, Mingyi Wang, Ruby Marten, Mihnea Surdu, Birte Rörup, Rima Baalbaki, Antonio Amorim, Farnoush Ataei, David M. Bell, Barbara Bertozzi, Zoé Brasseur, Lucía Caudillo, Dexian Chen, Biwu Chu, Lubna Dada, Jonathan Duplissy, Henning Finkenzeller, Manuel Granzin, Roberto Guida, Martin Heinritzi, Victoria Hofbauer, Siddharth Iyer, Deniz Kemppainen, Weimeng Kong, Jordan E. Krechmer, Andreas Kürten, Houssni Lamkaddam, Chuan Ping Lee, Brandon Lopez, Naser G. A. Mahfouz, Hanna E. Manninen, Dario Massabò, Roy L. Mauldin, Bernhard Mentler, Tatjana Müller, Joschka Pfeifer, Maxim Philippov, Ana A. Piedehierro, Pontus Roldin, Siegfried Schobesberger, Mario Simon, Dominik Stolzenburg, Yee Jun Tham, António Tomé, Nsikanabasi Silas Umo, Dongyu Wang, Yonghong Wang, Stefan K. Weber, André Welti, Robin Wollesen de Jonge, Yusheng Wu, Marcel Zauner-Wieczorek, Felix Zust, Urs Baltensperger, Joachim Curtius, Richard C. Flagan, Armin Hansel, Ottmar Möhler, Tuukka Petäjä, Rainer Volkamer, Markku Kulmala, Katrianne Lehtipalo, Matti Rissanen, Jasper Kirkby, Imad El-Haddad, Federico Bianchi,* Mikko Sipilä, Neil M. Donahue, and Douglas R. Worsnop

Cite This: *Environ. Sci. Technol.* 2022, 56, 13931−13944

Read Online

ACCESS | Metrics & More | Article Recommendations | Supporting Information

ABSTRACT: Dimethyl sulfide (DMS) influences climate via cloud condensation nuclei (CCN) formation resulting from its oxidation products (mainly methanesulfonic acid, MSA, and sulfuric acid, H_2SO_4). Despite their importance, accurate prediction of MSA and H_2SO_4 from DMS oxidation remains challenging. With comprehensive experiments carried out in the Cosmics Leaving Outdoor Droplets (CLOUD) chamber at CERN, we show that decreasing the temperature from +25 to −10 °C enhances the gas-phase MSA production by an order of magnitude from OH-initiated DMS oxidation, while H_2SO_4 production is modestly affected. This leads to a gas-phase H_2SO_4-to-MSA ratio (H_2SO_4/MSA) smaller than one at low temperatures, consistent with field observations in polar regions. With an updated DMS oxidation mechanism, we find that methanesulfinic acid, $CH_3S(O)OH$, MSIA, forms large amounts of MSA. Overall, our results reveal that MSA yields are a factor of 2−10 higher than those predicted by the widely used Master Chemical Mechanism (MCMv3.3.1), and the NO_x effect is less significant than that of temperature. Our updated mechanism explains the high MSA production rates observed in field observations, especially at low temperatures, thus, substantiating the greater importance of MSA in the natural sulfur cycle and natural CCN formation. Our mechanism will improve the interpretation of present-day and historical gas-phase H_2SO_4/MSA measurements.

KEYWORDS: dimethyl sulfide (DMS), OH-initiated oxidation, methanesulfonic acid (MSA), methanesulfinic acid ($CH_3S(O)OH$, MSIA), low temperatures
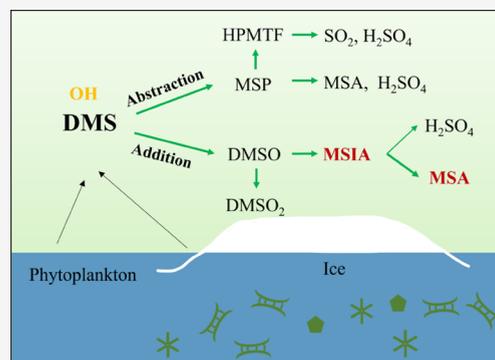
INTRODUCTION

Dimethyl sulfide (DMS) is emitted into the atmosphere by marine bacteria and as a result of the degradation of dimethylsulfoniopropionate (DMSP) produced from phytoplankton.[1−3] These emissions are the most abundant biological source of sulfur,[3] contributing between 18 and 42% of the global atmospheric sulfate aerosol.[4] Sulfur-containing oxidation products from DMS—specifically, sulfuric acid (H_2SO_4) and

methanesulfonic acid ($CH_3S(O)(O)OH$, MSA) that formed in the gas phase and condensed phase—take part in the formation of sulfur-containing aerosols and cloud condensation nuclei (CCN) in the marine atmosphere.[3,5−7] They initially form small (ca. nanometer-sized) molecular clusters through nucleation,[8−13] after which they grow by further condensation to CCN sizes. They thus affect the formation, optical properties, and lifetime of marine clouds,[8] influencing cloud radiative properties and therefore climate.[5,14−16]

The ratio of particulate MSA to non-sea-salt sulfate varies between 0.05 and 0.75 and is usually below 0.5.[6,7,17,18] Understanding how gaseous MSA contributes to this ratio is important in understanding the impact of DMS oceanic emissions leading to the formation of low-volatility species via oxidation. The multiphase chemical mechanism is complex, and the yields of H_2SO_4 and MSA depend on temperature[19] as well as atmospheric composition. Moreover, field measurements of gas-phase MSA and H_2SO_4 show a wide range of concentrations.[12,20−23]

Atmospheric MSA is formed primarily from DMS oxidation, with high concentrations observed in polar regions.[12] Atmospheric H_2SO_4 is formed from sulfur dioxide (SO_2) oxidation, which comes from anthropogenic and volcanic emissions as well as DMS oxidation. It follows that the ratio of H_2SO_4 to MSA (H_2SO_4/MSA) is an important indicator of both regional variations and anthropogenic perturbation in both current and historical samples. Furthermore, both species may participate in new particle formation[8−13] and CCN formation processes together with iodine oxoacids and ammonia in polar regions.[24,25] Consequently, a quantitative, mechanistic understanding of the DMS oxidation mechanism(s), especially the resulting H_2SO_4/MSA, is essential to further our understanding of their roles in climate change.

DMS oxidation has been studied extensively with a wide array of instrumentation. However, chamber and flow-tube experiments have had difficulties reproducing DMS oxidation under atmospherically representative conditions, leaving us with significant gaps in our chemical understanding.[26−28] Recent experimental work and in situ field observations have shown that autoxidation plays an important role in the oxidation of DMS at higher temperatures (>0 °C), proceeding through the formation of hydroperoxymethyl thioformate (HPMTF; $HOOCH_2SCHO$) via isomerization of the methylthiomethylperoxy radical (CH_3SCH_2OO, MSP), which is the primary product of DMS hydrogen abstraction.[29−32] However, subzero conditions (<0 °C) are challenging to investigate experimentally and so have received less attention. Hydrogen abstraction, both by OH and via isomerization (autoxidation), is suppressed at a lower temperature, and the OH addition pathway is known to dominate, as shown in previous studies.[33−35] Finally, wall reactions can be problematic in the laboratory, and their effects on the DMS oxidation experiments have been unclear so far.[27]

Model studies have addressed the importance of halogen chemistry[36−39] and aqueous-phase processes[28,37,38,40] to close the gaps between the modeled and measured oxidation products, suggesting reduced importance for OH-initiated DMS oxidation. However, even with recent revisions based on experimental findings, models with current state-of-the-art gas-phase mechanisms underestimate ambient MSA.[37,40] Here, we show that those mechanisms overestimate H_2SO_4/MSA by a factor of 2−10 throughout the ambient temperature range. The mechanism adopted in this study is similar to the gas-phase mechanism in the study of Wollesen de Jonge et al.,[41] which revised the gas-phase chemistry (MCM) to explain their high particulate MSA.

We performed experiments in the CLOUD chamber at CERN[13] under conditions that closely match the marine boundary layer (MBL) with an extensive suite of instruments. We investigated the gas-phase OH-initiated DMS oxidation over a wide temperature range (−10 to +25 °C) and present a revised mechanism describing gas-phase DMS oxidation. In addition to H_2SO_4 and MSA, we quantified numerous intermediate products, including the key intermediate methanesulfinic acid ($CH_3S(O)OH$, MSIA), and used them to evaluate and constrain the mechanism. In addition to the gas-phase chemistry, we quantified semiempirical rate coefficients for the heterogeneous formation of the important products dimethyl sulfoxide ($CH_3S(O)CH_3$, DMSO) and dimethyl sulfone ($CH_3S(O)_2CH_3$, DMSO$_2$). We designed our experiments such that the particle condensation sink (CS) is negligible. In CLOUD and most experiments, these multiphase processes occur on the chamber walls,[27,41] but they can also occur on or within aerosols and cloud droplets in the atmosphere. We investigated the effects of temperature and NO_x on gas-phase OH-initiated DMS oxidation. Both our experiments and our revised oxidation mechanism closely match ambient gas-phase H_2SO_4/MSA, and together they provide a quantitative understanding of this critical natural biogeochemical process.

■ MATERIALS AND METHODS

CLOUD Chamber and Experiments. The CLOUD chamber is an electropolished stainless steel cylinder with a volume of 26.1 m^3. The chamber is surrounded by an insulated thermal housing, which maintains high-temperature uniformity and stability, and it can be operated over a wide range of temperatures (from −70 to +100 °C) and relative humidity (from below 1% to above 90%). Ultrapure synthetic, humidified air (cryogenic 79% N_2 and 21% O_2) and a slight overpressure minimize contaminants in the chamber. All trace gases (e.g., SO_2, O_3, CO, NH_3, NO_x, and DMS) have independent gas lines connected to the chamber to avoid reactions caused by mixing in the gas lines before injecting into the chamber. Dry nitrogen was used to dilute DMS, NO_2, and O_3 from standard high-concentration gas bottles before reaching the chamber to obtain close to atmospheric concentrations.

Four 200 W Hg−Xe UV lamps (UVH LC8, Hamamatsu Photonics K.K., Japan) at wavelengths between 250 and 450 nm with adjustable power and a xenon fluoride excimer laser (UVX) at 248 nm were used to generate OH radicals via photolysis of ozone (O_3). The distribution of UV lamps and laser in the chamber make the gas-phase oxidation products (e.g., OH) form uniformly in a few minutes. An LED sabre (LS3) at 385 nm was used to photolyze NO_2 producing NO. Sulfur dioxide (SO_2) was measured with a high-sensitivity pulse fluorescence analyser (model 43i-TLE; Thermo Fisher Scientific), ozone with a UV photometric ozone analyser (model 49C; Thermo Environmental Instruments), carbon monoxide using a nondispersion cross-modulation infrared analysis method (model APMA-370; Horiba), and nitrogen oxides NO with an ECO Physics CLD 780TR and NO_2 with a Cavity Enhanced Differential Optical Absorption Spectroscopy (CE-DOAS). The SO_2 monitor employed at CLOUD was unfortunately not able to measure the formed SO_2 from DMS

oxidation because of its high detection limit (0.5 ppb). A chilled dew-point mirror (EdgeTech Instruments) and a direct tunable diode laser absorption spectrometer (TDL hygrometer, Werle et al.[42]) were used to continuously monitor the water vapor concentration.

The OH-initiated DMS oxidation experiment was conducted as follows: Before the oxidation experiments, the mixing fan speed was set to 100% to enhance turbulent mixing in the chamber, thus reducing the concentrations of oxidation products due to faster wall loss. The injection rates of ozone, DMS, and NO_x were set to reach the desired values. The experiment was then initiated by switching the UV lights on and setting the fan speed to 12% to initiate DMS oxidation (by OH radicals) and to reduce wall loss rates of DMS oxidation products to establish a new steady-state condition. Temperature-ramping experiments were conducted at two temperature ranges (+25 to +10 and +10 to −10 °C) with different initial concentrations of DMS, OH, and CO. The temperature ramps took a few hours each, which is only slightly longer than the residence time in the chamber. Therefore, unlike in a typical oxidation experiment, steady states were not reached for each temperature in the temperature-ramping experiments. As such, H_2SO_4-to-MSA ratios in these experiments should not be used directly in other contexts because they are not measured in steady state. They can, however, be used for investigating the temperature dependence by simulating the full concentration profile at each point in time and then comparing the model results with the experimental results.

Measurements of DMS and its Oxidation Products. State-of-the-art instruments were operated simultaneously to measure the gas-phase concentrations of DMS and its oxidation products. They were measured by a suite of advanced mass spectrometers including a nitrate-ion-based chemical ionization mass spectrometer (NO_3^--CIMS), a bromide chemical ionization mass spectrometer coupled with a multischeme chemical ionization inlet (Br$^-$-MION-CIMS), the gas-phase channel of a bromide chemical ionization mass spectrometer equipped with a Filter Inlet for Gases and AEROsols inlet (Br$^-$-FIGAERO-CIMS), selective reagent ionization mass spectrometers (SRI-TOF-MS), and proton-transfer reaction time-of-flight mass spectrometer (H_3O^+-CIMS, NH_4^+-CIMS). The experiments were grouped into three sets depending on the availability of instruments and temperature. We conducted experiment set 1 at −10 °C, experiment set 2 at +10 and −10 °C, and experiment set 3 at +25 and +10 °C, with relative humidity ranging from 20 to 70%. NO_3^--CIMS and PTR3 worked during all of the experiments. However, the mode of PTR3 was changed from a regular H_3O^+ mode to NH_4^+ mode in experiment set 3. Br$^-$-MION-CIMS measurements were only available in experiment set 1 and Br$^-$-FIGAERO-CIMS measurements were only in experiment set 2. The conditions of the experiments and relevant instruments are listed in Table S1.

DMS. A proton-transfer reaction time-of-flight mass spectrometer (H_3O^+-CIMS) provided the DMS concentration. The instrument is based on the design of the proton-transfer reaction time-of-flight mass spectrometer (PTR3) described in Breitenlechner et al.[43] DMS concentrations were calibrated with a gas standard at specific conditions between experiments. The concentrations of DMS for the second experiment set were provided by the selective reagent ionization mass spectrometer (SRI-TOF-MS) described in detail by Canaval et al.[44] We calibrated both instruments regularly between

experiments with a standard gas mixture containing multiple volatile organic compounds to account for any possible drifts in transmission efficiency or absolute humidity dependency.

H_2SO_4, MSA, and $CH_3S(O)_2OOH$. The concentrations of H_2SO_4, MSA, and $CH_3S(O)_2OOH$ were measured with a nitrate-ion-based chemical ionization mass spectrometer (NO_3^--CIMS; Tofwerk AG, Thun, Switzerland; Jokinen et al.[45]). The specially designed inlet for chemical ionization at the ambient pressure system and its calibration and quantification procedures are well described by previous studies.[46,47] We applied the same calibration coefficient $C_{H_2SO_4}$ = 4.13 × 10^{10} cm^{-3} per normalized signal (cps cps^{-1}; cps denotes counts per second) for the experiments carried out at +10 and −10 °C since charging efficiency does not vary significantly in this temperature range. The uncertainty for NO_3^--CIMS is mainly caused by H_2SO_4 calibration, below ∼50%; this uncertainty includes the systematic error from calibration setup and statistic error. All uncertainties for each species from the different instruments are listed in Table S2. We estimate that MSA has a collision-limited charging efficiency and strong binding energy with less fragmentation than H_2SO_4 based on the cluster binding enthalpy calculated by quantum chemical methods (see Text S1.3 and Tables S3 and S4 for details). The measurement sensitivity of methanesulfonic peroxide ($CH_3S(O)_2OOH$) is lower than the maximum sensitivity, and the given concentrations represent its lower limits. The detailed estimation for MSA and $CH_3S(O)_2OOH$ can be found in Text S1.3.

DMSO, $DMSO_2$, CH_3SCHO, and CH_3SOH. The concentrations of DMSO, $DMSO_2$, methyl thioformate (CH_3SCHO), and methanesulfenic acid (CH_3SOH) were measured either by an H_3O^+- or NH_4^+-CIMS.[48] Different ionization schemes (H_3O^+- or NH_4^+-chemical ionization) were used in different experiments as shown in Table S1. We determined the instrument's collision limit calibration factor by ionizing 1 ppbv of hexanone from a gas standard diluted in air. Applying the collision limit calibration factor to all compounds ensures lower-limit estimates for their concentrations. As shown in Figure S2, the independence of the concentration ratios determined by both ionization methods (H_3O^+- and NH_4^+-chemical ionization) with the collision limit calibration factor on sample gas humidity and temperature suggests that both DMSO and $DMSO_2$ are very likely ionized at the collision limit in both ionization modes. The lower-limit estimates are therefore most likely their true concentrations. The comparison between the two ionization methods at the same time can be realized with additional experiments performed with high ammonia concentration in the chamber. These additional experiments have much higher DMS, O_3, and NH_3 concentrations than the OH-initiated DMS oxidation experiments to investigate the formed particles at larger sizes of around 100 nm. In contrast to the OH oxidation experiments whose goal is to investigate the chemical mechanism, the goal of the additional experiments with high NH_3 is to investigate the CCN potential of the formed particles. That is, the much higher concentrations of DMS, O_3, and NH_3 facilitate sustained condensation that leads to larger particles. Additionally, the conducted voltage scan experiment in Figure S3 shows that the DMSO and $DMSO_2$ hydronium-water and ammonium clusters are stable against fragmentation at the chosen settings and that their proton affinity is high enough to even keep the charge upon collision-induced fragmentation at

higher voltages. Their uncertainties are estimated at around 20% in H_3O^+-CIMS and 50−80% in NH_4^+-CIMS with the larger uncertainty of the collision limit sensitivity in the latter. The reported concentrations of CH_3SCHO and CH_3SOH are lower-limit estimates also based on the results of the voltage scans. See Text S1.4 for the detailed description.

HPMTF and MSIA. A bromide chemical ionization mass spectrometer coupled with a multischeme chemical ionization inlet (Br⁻-MION-CIMS) and the gas-phase measurement of bromide chemical ionization mass spectrometer equipped with a Filter Inlet for Gases and AEROsols (Br⁻-FIGAERO-CIMS)[49] were the primary instruments to detect MSIA and HPMTF. The peaks of MSIA and HPMTF measured by Br⁻-MION-CIMS can be found in Figure S4. If neither instrument was available due to instrument malfunction or absence in some experiments, NO_3^--CIMS was used to measure MSIA and HPMTF. The instrument setup and operation of Br⁻-MION-CIMS and FIGAERO are described in Rissanen et al.[50] and Lopez-Hilfiker et al.,[49] respectively. In addition to ionization with Br⁻, we also detected both MSIA and HPMTF with NH_4^+ and H_3O^+-CIMS. While direct calibrations of MSIA and HPMTF were not available, the intercomparison between the three ionization modes and the use of quantum chemical calculations provide reasonable constraints on the ionization efficiency of the two species and hence their concentrations.

We first derived MSA calibration coefficients for Br⁻-MION-CIMS and Br⁻-FIGAERO$_{(g)}$-CIMS using the MSA concentration measured by NO_3^--CIMS. Afterward, MSA calibration factors in both instruments are used to estimate the lower limits of HPMTF and MSIA concentrations with high uncertainty. The traces shown in Figure S7 for MSIA from NH_4^+- and H_3O^+-CIMS are calibrated using the collision limit assumption. It is very likely that if ionization does not occur at the collision limit with all primary ion clusters with water, a strong water dependence would be observed between the different modes. The apparent humidity independence of the ratio of the MSIA concentration derived from the three different ionization schemes (NH_4^+, H_3O^+, and Br⁻) suggests that the compound is detected at the collision limit in these ionization schemes. However, the fragmentation caused by the electric field in the vacuum chamber also affects the detection efficiency. The signals of MSIA and HPMTF in Br⁻-MION-CIMS might underly some fragmentation or other unaccounted losses in the instrument or inlet. Yet, the voltage scan results in Figure S8 show that MSIA is detected at maximum sensitivity in both H_3O^+ and NH_4^+-CIMS. Therefore, we use the MSIA concentration from H_3O^+-CIMS with around 28% uncertainty due to the calibration and inlet and instrumental loss correction. The signal of HPMTF is influenced by neighboring peaks and is divided into many water clusters in H_3O^+-CIMS, while this is not the case in NH_4^+-CIMS. Unfortunately, NH_4^+-CIMS was not available for many of the experiments, and the limit of detection in H_3O^+-CIMS was too high to use the data during the herein analyzed experiments with low concentrations. As such, we use the lower-limit estimation for HPMTF concentrations from Br⁻-FIGAERO$_{(g)}$-CIMS. See Section S1.5 for the detailed description and estimations.

Steady-State Measurement and Production Rate Calculation. The average residence time in the CLOUD chamber was ~1.3 h for experiment sets 1 and 2. The reaction rates of oxidation products were derived from steady-state measurements, which means that the inflow of all gases, the concentration of oxidants, and oxidation products were kept constant. Under steady-state conditions, the rate of change of oxidation products equals zero, and we can write

$$\frac{d[X]}{dt} = p - [X] \times k_{loss} - \sum_i k_{Y_i} \times [Y_i] \times [X] = 0 \tag{1}$$

Therefore, we can get the production rate p

$$p = [X] \times k_{loss} + \sum_i k_{Y_i} \times [Y_i] \times [X] \tag{2}$$

where X is the oxidation product, Y typically is OH or O_3, k_{Y_i} are the reaction rate coefficients for the reaction of X and Y, and k_{loss} is either the ventilation loss (2.1×10^{-4} s⁻¹ in experiment sets 1 and 2) or wall loss that is listed in Table S2. All of the oxidation product concentrations were measured at the steady-state condition. The OH concentration used in this study is estimated from our box model, and its reactions involved in forming OH radicals are listed in Table S7.

Modeling. In this study, a numerical model with zero dimension was set up and used to simulate DMS oxidation processes at different initial conditions (Table S1). We combine the simulation and experimental results to evaluate and constrain the role of different DMS gas-phase oxidation pathways in MSA and H_2SO_4 formation. The chemistry mechanism was generated with the Kinetic PreProcessor (KPP)[51] and solved with the ordinary differential equation solver RODAS3 (Rosenbrock method of order 3).[52] The concentrations of oxidation products are determined by the chemical production and loss from gaseous chemistry, wall reactions, ventilation loss, wall loss, and the condensation sink (CS) to generate particles in the CLOUD chamber. The measured temperature, relative humidity, DMS, O_3, CO, NO_x concentrations (Table S1), and O_3 photolysis rate with high time resolution were used as input to the model. The photolysis rate of O_3 for UVH at full intensity or 5 W of UVX is around 6×10^{-5} s⁻¹. The OH concentrations are adjusted by changing the UV light intensity, O_3, and H_2O concentrations. The CLOUD chamber ventilation loss is mainly determined by the flush-out flow (~330 lpm in experiment sets 1 and 2, 250 lpm in experiment set 3). Species like H_2SO_4, MSA, and hydrogen oxide radicals are readily lost to the wall surface. We measured the lifetime of all species (Table S2) in the dark decay (lights off, fan 12%) and cleaning stage (lights off, fan 100%) to estimate the losses and applied them to our box model. With the increase of fan speed from 12 to 100%, the wall losses increased by a factor of 1.5−4.6 for different species. The measured loss of species like methyl thioformate (CH_3SCHO) in the cleaning stage is slightly larger than the ventilation loss caused by the flush-out flow. It suggests that the loss of CH_3SCHO is dominated by ventilation whose loss increases mildly with the increased fan speed. Therefore, we added extra loss terms for dimethyl sulfoxide ($CH_3S(O)CH_3$, DMSO), dimethyl sulfone ($CH_3S(O)_2CH_3$, $DMSO_2$), and CH_3SCHO to fit their time evolutions in the cleaning stage. The particle condensation sink measured in this study is smaller than 1×10^{-5} s⁻¹, which is negligible compared to other loss processes. The detailed description of chemistry mechanisms used in the box model can be found in Text S2.
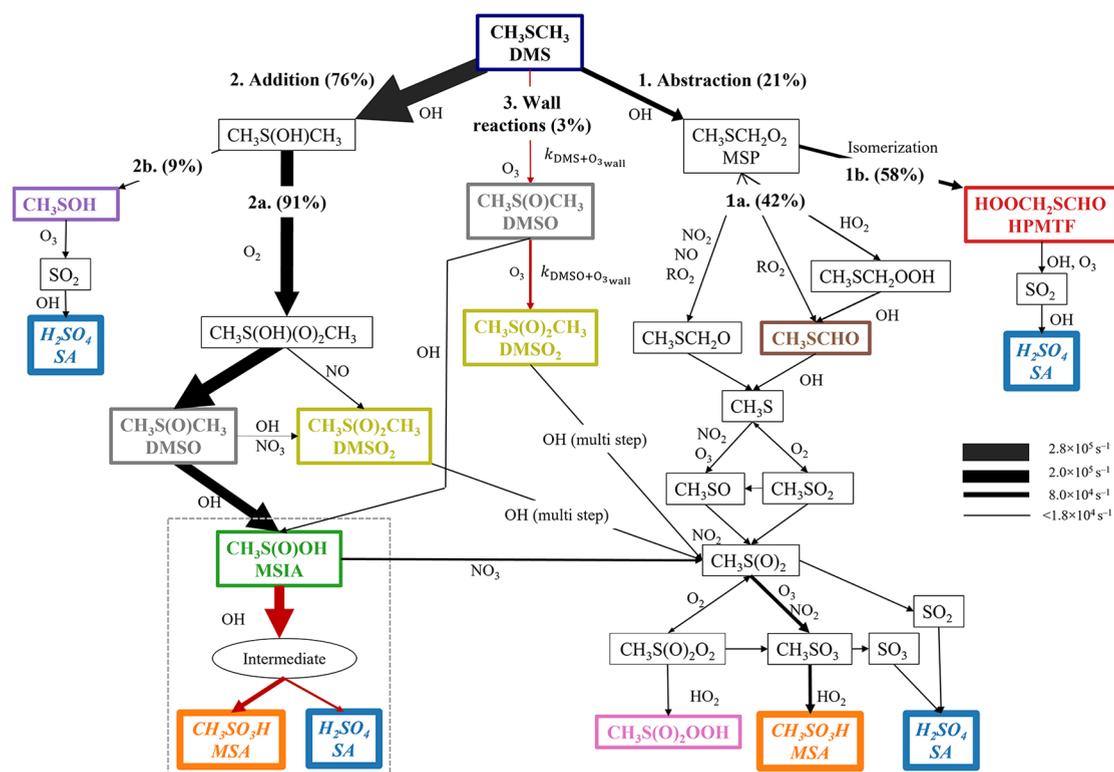
Figure 1. Schematic representation of DMS oxidation with OH radicals in this study. Most reactions are taken from MCMv3.3.1, Hoffman et al., and recent publications.[29,31,32,41] The widths of the arrows indicate production rates (s^{-1}) on a linear scale, which arecalculated at $-10\ °C$ with 100 pptv DMS, $7 \times 10^6\ cm^{-3}$ OH, 40 ppbv O_3, 2 pptv NO, and 200 pptv NO_2. We set the same width for reaction rates when they are below 1.8×10^4 s^{-1}. The percentage given for each pathway indicates the branching ratio of the production rates at this condition. The precentage of MSP leads to pathways 1b is temperature-dependent. At $+22\ °C$, the reaction follows pathway 1b to 97%. The reaction rate coefficients of the isomerization of MSP are discussed in Text S2. Red arrows highlight the important reactions proposed in this study. The mechanism of MSIA reacts with OH surrounded by the thin, dashed gray line is the possible alternative formation mechanism we suggest but their reaction rate coefficients are not fully studied. Therefore, we treat the MSIA converting to $CH_3S(O)_2$ in our box model. $k_{DMS\ +\ O_{3wall}}$ and $k_{DMS\ +\ O_{3wall}}$ are the semiempirical reaction rate coefficients for heterogeneous wall reactions (see Text S4 for details). The species in colored boxes in this figure are those we quantify, and the color of each box outline matches the color of each time trace in Figure 2. Species $CH_3S(OH)CH_3$, $CH_3S(O_2)(OH)CH_3$, CH_3SCH_2O, CH_3SO, and CH_3SO_2 have not been measured before but are included here based on modeling studies.[33,35,40]

■ RESULTS

Identification of Oxidation Products from OH-Initiated DMS Oxidation. Figure 1 shows an oxidation mechanism initiated by the DMS + OH reaction and informed by the experiments we describe here, and Figure 2 shows an example time series of measured species for an experiment conducted at $-10\ °C$ with NO_x below the instrument detection limit, $\lesssim 2$ pptv. With sensitive chemical ionization mass spectrometers, we are able to identify and quantify many intermediates and terminal products in this mechanism. The species we measure include MSA and H_2SO_4, as well as DMSO, DMSO$_2$, MSIA, and HPMTF. These are the major sulfur-containing products also previously identified and measured from DMS oxidation.[26,27,29,32,53] We also identify $CH_3S(O)_2OOH$, CH_3SCHO, and CH_3SOH, as shown in the figures. Some species are quantified with proper calibration factors, while species like $CH_3S(O)_2OOH$, HPMTF, CH_3SOH, and CH_3SCHO (by NH_4^+-CIMS) are lower-limit estimates due to the lack of authentic standards or generation methods. A more detailed description is given in the Materials and Methods section and Text S1.

The time traces in Figure 2 show the sequence of a typical experiment, starting with the characterization of wall losses in the dark, followed by the initiation of photochemistry. UV

lights, the trigger of OH radicals, were switched on at midnight (00:00) after DMS and ozone (O_3) concentrations stabilized. The time sequences of different DMS oxidation products show different behaviors. The evolution of H_2SO_4, MSA, MSIA, HPMTF, $CH_3S(O)_2OOH$, and CH_3SOH is consistent with the expected time response of gas-phase production through OH oxidation (with lights on) and wall loss. The measured concentration reaches their maxima in the order of a few minutes rather than a few hours like aqueous-phase reactions. The CH_3SCHO evolution is consistent with gas-phase production and loss to ventilation rather than the walls, which has a timescale of ~1.3 h (26.1 m^3/330 lpm). DMSO shows a small fractional, but large absolute, increase with photochemistry, yet only a modest fractional wall loss. DMSO rapidly reaches a steady state, while DMSO$_2$ decreases slowly and continuously from the onset of the run, associated with the slowly decreasing product of the DMS and O_3 concentrations.

Mechanism Treatment via the Box Model. Figure S11 reveals that DMSO and DMSO$_2$ have a source from the wall, which has also been shown in a previous study.[27] As described in the Methods section, we first constrain wall effects to delineate gas-phase chemistry; however, the gas-phase photochemistry is dominant for all species other than DMSO$_2$ when the UV lights are on. In turn, DMSO$_2$ is long-lived in the gas
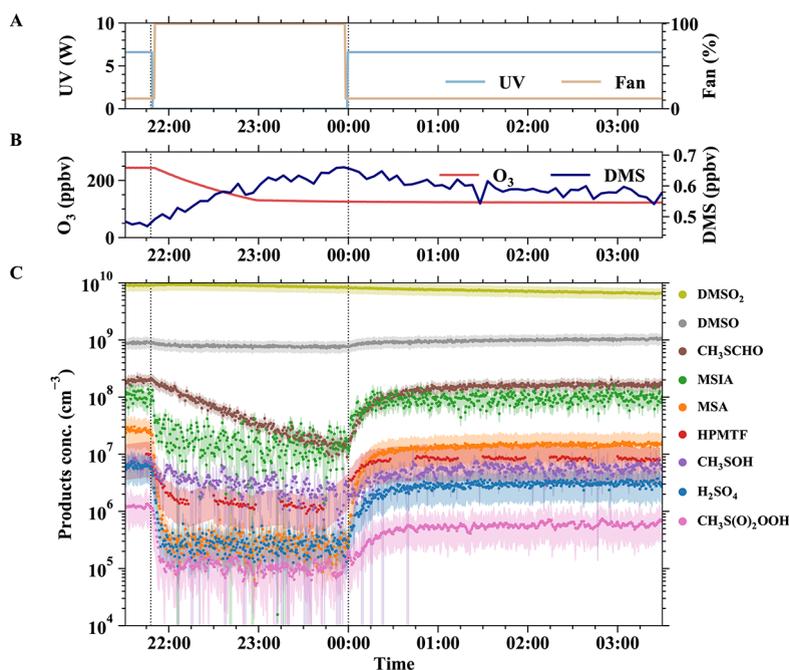
Figure 2. Experiment of OH-initiated DMS oxidation at -10 °C. (A) Time series of ultraviolet light intensity (blue line, left axis; used to photolyze O_3 to produce OH radicals) and mixing fan speed to accelerate wall losses (orange line, right axis). (B) O_3 (red line, left axis) and DMS (navy line, right axis) concentrations. (C) Measured DMS oxidation products (solid dots, colors correspond to box outlines in Figure 1). After a brief period ended at 21:48, UV lights were turned off and the fan speed was increased to full intensity to encourage wall losses. Most species were removed efficiently and showed a sharp drop. However, the loss of CH_3SCHO was mainly due to the chamber ventilation (with a dilution lifetime of 1.3 h). $DMSO_2$ was relatively insensitive to fan change since it was primarily produced from heterogeneous production on the walls, while DMSO was less affected by multiphase reactions (primarily from gas-phase reactions). When the fan speed was lowered and UV lights were turned on, the concentrations of most species increased due to OH oxidation of DMS. The shade for each time series presents the uncertainty of each species except for the species (HPMTF, $CH_3S(O_2)OOH$, and CH_3SOH) whose concentrations are lower-limit estimates; their uncertainty only includes the instrumental loss without correction from sensitivity.

phase and so has minimal influence on the chemistry. DMSO is also produced on the walls, but once OH is present, both gas-phase production and loss of DMSO via OH far exceed the wall production rate (see Text S4 and Figure S11).

As shown in Figure 2, the terminal products MSA and H_2SO_4 are far less abundant than the first-generation oxidation product CH_3SCHO, but MSA and H_2SO_4 have rapid wall loss, as do their precursors, such as MSIA, CH_3SOH, and HPMTF. Considering the wall loss rate, we find that the production rates for MSA (3.2×10^4 s^{-1}) and CH_3SCHO (4.5×10^4 s^{-1}) are similar, with uncertainties at around 50 and 20%, mainly caused by their measured concentrations. We seek these production rates along with molar yields and branching ratios. To constrain the production rates, we need a photochemical model of the chamber and the DMS oxidation sequence, including the walls.

The measured wall losses in Table S2 show that MSA and H_2SO_4 have the same values, allowing a direct comparison of the two species' concentrations. As shown in Figure 2, the measured MSA is high and 3.7 times larger than H_2SO_4, which cannot be explained when assuming that MSA is exclusively formed from the hydrogen abstraction channel (pathway 1 in Figure 1). We observe a positive relationship between MSIA and MSA, shown in Figures S12 and S13. Previous studies[54,55] have concluded that SO_2 is the lone major product of the reaction of OH with MSIA. However, the abstraction of an acidic H-atom by OH radicals is typically slow because acidity implies a deficiency in electron density.[56] By contrast, OH addition to the S-atom in MSIA is more likely to produce an

intermediate product that may decompose to form sulfurous acid (H_2SO_3) and CH_3,[55] but may also react with O_2 to produce MSA. This pathway and its reaction rate coefficients are not yet well understood. Therefore, in the box model, we add the pathway proposed by Yin et al.,[57] Lucas et al.,[58] and Hoffmann et al.[40] that MSIA reacts with OH or NO_3 radicals forming methyl sulfonyl radicals ($CH_3S(O)_2$) as an intermediate, which then either decomposes to SO_2 or reacts with O_3 to form MSA (via CH_3SO_3 reaction with HO_2) and SO_3, instead of producing SO_2 only. A recent study also applied this pathway to a multiphase model[41] to explain the observed high particulate MSA/sulfate at 0 and 20 °C.

Lv et al.[55] suggested that the reaction of MSIA and O_3 is unlikely to be competitive with MSIA and OH because of the large discrepancy between these two reaction rate coefficients. Even at high O_3 concentrations (ca. 100 ppbv), the first-order reaction rate coefficient of MSIA by O_3 is 4.4×10^{-10} s^{-1}, which is much smaller than the first-order reaction rate coefficient of MSIA by OH at 2.8×10^{-4} s^{-1} (with lowest OH concentrations, $\sim 1 \times 10^6$ cm^{-3}). Therefore, the critical conclusion is that we would suggest that MSIA reacts with OH, producing both MSA and H_2SO_4. Thus, both the addition and abstraction pathways of DMS oxidation form MSA in the gas phase, explaining the higher MSA concentrations observed in field observations and CLOUD experiments.

To treat wall effects, we add wall reactions as pathway (3) to our DMS oxidation mechanism (Figure 1) by directly applying two semiempirical rate coefficients $k_{DMS + O_{3wall}}$ and $k_{DMSO + O_{3wall}}$.
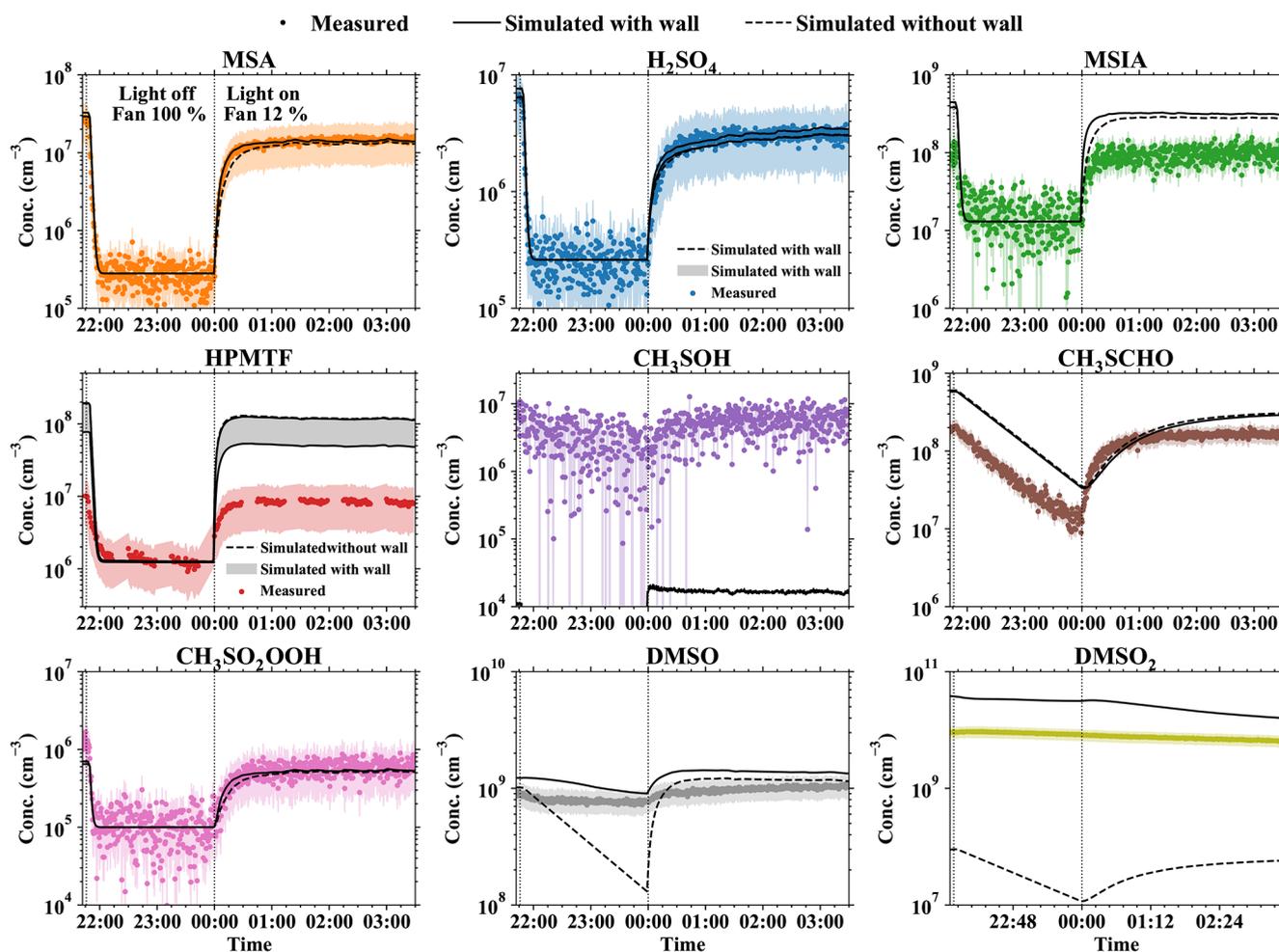
Figure 3. Measured and modeled gas-phase concentrations of identified species at an OH-initiated DMS oxidation experiment. Circles are the identified species measured by NO_3^--CIMS, H_3O^+-CIMS, and Br^--FIGAERO$_{(g)}$. Solid lines represent simulation results, including wall reactions of DMSO and DMSO$_2$ and dashed lines represent simulation results excluding wall reactions. Wall loss is included in our box model; therefore, we can compare the measured and simulated values directly. The differences between the modeled and measured HPMTF and CH$_3$SCHO are mainly because they are lower-limit estimates (see Texts S1.4 and S1.5 for quantitative measurement), which means their concentrations are underestimated in this case. The shadow area in the subplot of HPMTF presents the variation caused by applying different reaction rate coefficients of isomerization of MSP. Since the production rate of CH$_3$SOH is unclear, the simulated CH$_3$SOH concentrations are much lower than the measured values. It is a coincidence for the agreement between the measured and simulated CH$_3$SO$_2$OOH concentrations (lower-limit estimates), but we do not investigate it in detail because it is not important for understanding MSA and H$_2$SO$_4$ formation. The shade for each time series presents the uncertainty of each species except for the species (HPMTF, CH$_3$S(O$_2$)OOH, and CH$_3$SOH) whose concentrations are lower-limit estimates; their uncertainty only includes the instrumental loss without correction from sensitivity.

Using a numerical model (see Material and Methods for the configuration and mechanism), we then evaluate the proposed mechanism herein. We compare the measured oxidation products (circles) with their modeled values, including wall reactions (solid lines) in Figure 3 for the same OH-initiated DMS oxidation experiment as Figure 2.

The modeled MSA, H$_2$SO$_4$, CH$_3$S(O)$_2$OOH, and DMSO concentrations in Figure 3 are within 50% uncertainty of the measured values. The time evolution of HPMTF and MSIA in the simulation follows the same trend as the measured values. The modeled MSIA concentrations exceed the measured value (within an uncertainty of 28%) by a factor of 3, which is believed to be reasonable due to the uncertainties in DMS chemistry, chamber loss parameterizations, and systematic measurement errors. The smallest discrepancy between the modeled and measured HPMTF is a factor of 6. This difference can be explained by the uncertainty and the reduced

sensitivity of the gas-phase measurement of Br$^-$-FIGAERO-CIMS to HPMTF due to a stronger declustering process compared to the maximum sensitivity compounds (see Text S1.5 for details). The discrepancy between the modeled and measured HPMTF can be varied from 6 to 14 by applying different reaction rate coefficients of the isomerization of MSP. As shown in Figure 3, the variation of HPMTF at low temperatures has a limited effect on DMS oxidation.

When we exclude the wall reaction from the model, the resulting vast difference between the modeled and measured DMSO$_2$ concentrations and their qualitative behaviors (Figure 3) indicates that wall reactions are essential to understanding the DMSO$_2$ formation. On the other hand, the simulation without wall interactions captures the time evolution of the other species except for DMSO, which indicates that OH-initiated DMS oxidation is their dominant source, and DMSO$_2$ is unlikely to be their primary precursor. The model suggests

that DMSO is formed for the most part from OH-initiated DMS oxidation in the gas phase but interacts strongly with the walls. The modeled DMSO concentrations are 54 and 46 pptv, with and without wall reactions, respectively. However, the temporal evolution of the concentration cannot be reliably predicted without wall interactions. As shown in Table S2, the uncertainties of measured MSA, H_2SO_4, MSIA, CH_3SCHO, DMSO, and $DMSO_2$ are below 50%. Although the uncertainties of HPMTF, CH_3SOH, and $CH_3S(O)_2OOH$ are high, their influences on our main conclusion—that MSA likely forms substantially via gas-phase oxidation of MSIA by OH—are negligible since they are not the determining species in this argument.

Overall, the underestimated calibration factor can explain the discrepancy between the modeled and simulated HPMTF. Based on the close agreement between the model and measurements for major oxidation products (DMSO, $DMSO_2$, MSIA, MSA, and H_2SO_4), we conclude that the mechanism presented here can represent DMS oxidation by OH radicals in the marine atmosphere.

Temperature Dependence for OH-Initiated DMS Oxidation. Temperature has a strong effect on (1) the branching ratio of addition/abstraction at the first step of DMS oxidation by OH radicals, (2) thermal decomposition of CH_3SO_2 and CH_3SO_3 in abstraction pathway 1a, (3), degradation of MSIA (which is not fully understood), and (4) peroxy radical isomerization of MSP in abstraction pathway 1b. All of these, especially the thermal decomposition, influence H_2SO_4/MSA. We plot H_2SO_4/MSA versus temperature in Figure 4 to present the temperature dependence for OH-initiated DMS oxidation. The green and red circles are from our CLOUD experiments with and without NO_x, respectively. The purple symbols are ambient data, and the black lines are box-model simulations with various mechanisms. The CLOUD data come from two separate temperature-ramping experiments, one cooling from +25 to +10 °C and the other from +10 to −10 °C, both without NO_x. In Figure 4, H_2SO_4/MSA ranges from 0.3 to 1.3 (−10 to +10 °C) and 1.4 to ~11 (+10 to +25 °C), decreasing exponentially with decreasing temperature. Ambient observations of gas-phase H_2SO_4/MSA vary from 1 to 17 at Mace Head, Ireland (during Summer)[21] and from 0.3 to 3 in polar regions (from February to August).[12] These observations can be reproduced by the inferred experimental temperature dependence. The ambient concentrations of DMS, O_3, OH, and NO_x during the measurements of H_2SO_4/MSA from Beck et al., presented in Figure 4, were, unfortunately, unknown and likely differed from our experimental conditions. The differences will inevitably influence the absolute MSA and H_2SO_4 concentrations reported in Beck et al.'s observation and our experiments. However, we find that the ratio of H_2SO_4/MSA is mainly determined by temperature (Figure 4) instead of precursor vapor concentrations, and therefore the H_2SO_4/MSA from our experiments is nonetheless used to compare with field observations. MSA formation has a stronger temperature dependence than H_2SO_4. A detailed discussion of the temperature dependence for all of the oxidation products is given in Text S5 and Figure S14.

We modeled the temperature dependence of H_2SO_4/MSA with the OH-initiated DMS oxidation mechanism developed here (solid line) and compare it to the gas-phase mechanism from MCMv3.3.1[59] (dashed line) and Hoffmann et al.[40] (dotted line) in Figure 4. These model results differ by up to
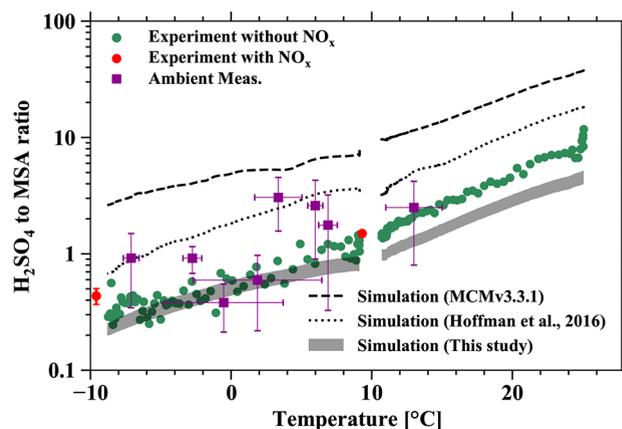

Figure 4. Temperature dependence of the H_2SO_4-to-MSA ratio. Green circles represent the H_2SO_4/MSA ratio without NO_x (green) from two temperature-ramping experiments measured by NO_3^--CIMS; red circles are the experimental H_2SO_4/MSA with NO_x. The NO_2 and NO differences between the red and green circles are around 400 and 8 pptv. The error bars represent the standard deviation of temperature and H_2SO_4/MSA. Purple square symbols are the daytime average of ambient measurement. They are the ambient measurements from 4 and 5 May, 5 and 6 August 2017 in Ny-Ålesund station, 20 August 2015 in Villum,[12] 16 and 17 December 2014 in ABOA station,[68] and 17 June 1999 in Mace head.[21] We decreased the temperature to study the temperature dependence, in contrast to increasing the temperature, to avoid the emission of contamination from the wall. Lines represent the simulation results using the OH-initiated gas-phase oxidation mechanism from MCMv3.3.1 (dashed line, with constant NO_x concentration) and Hoffman et al.[40] (dotted line). The simulation results in this study are presented as gray rectangles by varying the reaction rate coefficient of the isomerization of MSP.

an order of magnitude compared to the CLOUD measurements, but all show a similar exponential temperature dependence. This is because they all include thermal decomposition for $CH_3S(O)_2$ and CH_3SO_3 in abstraction pathway 1a, which contains an exponential temperature dependence that largely determines H_2SO_4/MSA. However, our mechanism shows much better agreement with the observed H_2SO_4/MSA compared to the other two mechanisms. This is because the reaction of MSIA with OH radicals contributes more to MSA production and consequently reduces H_2SO_4/MSA rather than only contributing to SO_2 formation, as e.g., in MCMv3.3.1. Overall, the observed temperature effect suggests a potentially greater role for MSA in colder regions in important processes such as new particle formation and growth, as our mechanism and observations show that the H_2SO_4/MSA ratio is smaller than 0.5 when the temperature is below roughly +2 °C.

Effect of NO_x on OH-Initiated DMS Oxidation. In addition to temperature, NO_x (i.e., NO_2 and NO) influences OH-initiated DMS oxidation, for example, through bimolecular reactions between peroxy radicals (RO_2) and NO. As shown in Figure 4, H_2SO_4/MSA from two experiments with NO_x (red circles) agrees with the temperature-ramping experimental results (green circles), indicating that NO_x has a negligible effect compared to the temperature sensitivity over this same range. The NO_x-ramping experiments in Figure S15 confirm that NO_2 and NO only slightly enhance H_2SO_4/MSA in contrast to the strong effect from temperature change. The measured H_2SO_4/MSA at +10 °C (Figure S15A) and −10 °C

(Figure S15B) increase by 54 and 100% as NO_2 increases from 0 to 400 pptv. The effect of NO_x on HPMTF formation is not clear (Figure S15). We observe a slight drop of HPMTF (17%) and almost constant DMS in Figure S15A. However, Figure S15B shows a 100% increase in HPMTF and a 20% drop in DMS because DMS reacts with NO_3 radicals. We cannot quantify the effect of NO_x on HPMTF formation because of the interference from N_2O_5 formed from the reaction of O_3 and NO_2, which has a close molecular weight to HPMTF.

In MCMv3.3.1, the modeled H_2SO_4/MSA (Figure S16) is very sensitive to NO_2 concentration varies dramatically as NO_2 increases from 0 to 160 pptv. However, the modeled H_2SO_4/MSA from the other two mechanisms (Figure 4) are insensitive to NO_x. In MCMv3.3.1, NO_2 constrains the formation of MSA through the reaction of CH_3SO with NO_2, which forms $CH_3S(O)_2$, because it excludes the isomerization reaction of CH_3SO_2 producing $CH_3S(O)_2$ (Hoffmann et al.[40]). The isomerization reaction is estimated with a constant value of ~1 s^{-1} in previous studies,[60,61] which is higher than the bimolecular reaction rate of CH_3SO with NO_2 (~1.2 × 10^{-1} s^{-1} with a maximum 400 pptv NO_2), although it lacks the temperature dependence.

Overall, the suite of simultaneously measured key intermediates helped us to adjust the previous DMS oxidation schemes. Our mechanism has two major improvements. First, the influence of NO_x on product distribution is greatly diminished compared to the MCMv3.3.1. Second, the key ratio H_2SO_4/MSA is substantially reduced (MSA is increased), with the absolute ratio and temperature dependence in the mechanism agreeing with both the experimental data and ambient observations.

■ DISCUSSION AND ATMOSPHERIC IMPLICATION

DMS oxidation in the atmosphere is affected by temperature, NO_x, the distribution of oxidants including OH, NO_3, halogen compounds,[36,37,62] and available water for multiphase oxidation in aerosols and droplets.[40,63] In this study, we followed the kinetics of a suite of gas-phase reaction intermediates and final products in DMS oxidation experiments by OH to investigate the effects of temperature and NO_x. Our results show a strong temperature dependence for DMS oxidation, especially the yields of oxidation products such as MSA.

Our experimental results show high MSA concentrations and reduced H_2SO_4/MSA from OH-initiated DMS oxidation, especially at low temperatures (<0 °C). From the box-model results, it is clear that the inclusion of the gas-phase MSA formation mechanism via oxidation of MSIA by OH improves the agreement between modeled and experimental results at low temperatures. When MSIA reacts with OH, it may produce $CH_3S(O)_2$ or another adduct intermediate; regardless, both $CH_3S(O)_2$ and the adduct intermediate decompose to SO_2 or SO_3 to form H_2SO_4 or react with O_3 or O_2 to form MSA. For both pathways, we can expect a similar temperature dependence.

At low temperatures, the oxidation of DMS with OH proceeds more via the OH addition channel, forming abundant DMSO and MSIA, and consequently, a large amount of MSA. At high temperatures, the reaction rate of the OH addition channel decreases, which lowers MSIA and MSA formation, while the hydrogen abstraction channel becomes more important. Also, the predominance of MSP isomerization (≥95, at 295 K)[29] leads to the HPMTF formation, which

increases H_2SO_4 production substantially through oxidation of HPMTF.[29,30]

Therefore, we propose that MSIA is important in MSA formation at low temperatures, which can also be connected to the observed high particulate MSA/sulfate in laboratory[41] and field observations[7,17] since both MSA and H_2SO_4 participate in particle growth. Interestingly, NO_x is far less influential than previously thought. At −10 °C, H_2SO_4/MSA increases by 100% after ramping up NO_2 (from 0 to 400 pptv) and NO (from 0 to 8 pptv). But the observed change (red circles) is small (less than 50%) compared to the effect of changing temperature (about an order of magnitude when the temperature decreases from +10 to −10 °C).

As shown in Table S5, our experimental MSA (0.2 to 1.5 × 10^7 cm^{-3}) and H_2SO_4 (0.3 to 3 × 10^6 cm^{-3}) concentrations formed from OH-initiated DMS oxidation experiments conducted at −10 °C are in the range of field measurements. For example, the concentrations of MSA and H_2SO_4 measured in Ny-Ålesund station (Figure S17, air temperature ranging from −10 to −7 °C) range from 0.1 to 4 × 10^7 cm^{-3} and 0.2 to 7 × 10^6 cm^{-3}, respectively. Aerosol concentrations also affect gas-phase MSA and H_2SO_4 concentrations because of their different aerosol partitioning. However, the particle condensation sink in this study is smaller than 1 × 10^{-5} s^{-1}, which is only slightly larger than the values at Ny-Ålesund (~4 × 10^{-4} s^{-1}) and Villum (~3 × 10^{-4} s^{-1}).

$DMSO_2$ and DMSO are important sulfur reservoirs in our study. They can also be formed from wall reactions without OH radicals. Our simulations show that wall reactions are the major source of $DMSO_2$ but have a limited role for other oxidation products compared to the gas-phase reactions (even DMSO). In the atmosphere, analogous to the wall of the chamber, cloud droplets and aerosol water could play a similar role. Therefore, the observed high concentrations of $DMSO_2$ (40−120 pptv) and DMSO (3−18 pptv) at night over the Arabian Sea[64] and Pacific Ocean[65] may be associated with multiphase DMS oxidation.

The DMS oxidation lasts only a few hours in the CLOUD chamber, while it can be for a few days in the atmosphere depending on the conditions. To gauge possible atmospheric evolution (a few days), we simulated OH-initiated DMS oxidation over a long timescale (~1 week) at −10 °C, excluding walls and ventilation. As shown in Figure S18, terminal products MSA and H_2SO_4 accumulate in parallel over time, ultimately constituting the dominant reaction products. DMSO, MSIA, CH_3SCHO, and CH_3SOH are the precursors for MSA and H_2SO_4, reaching a steady state during the first day of simulation. HPMTF is a precursor for SO_2, and after 1 week, both reach high concentrations and slowly approach steady state. Field measurements indicate high concentrations of HPMTF (up to 50 pptv in the marine atmosphere[32]) and its possible participation in particle formation. Accounting HPMTF chemistry in a global chemistry transport model[66] results in a significant decrease in boundary layer levels of SO_2 and H_2SO_4. Novak et al.[67] demonstrate that the rapid loss of HPMTF to clouds terminates DMS oxidation to SO_2. This is important at high temperatures. On the other hand, at low temperatures, HPMTF production is strongly reduced, and the main product becomes MSA via MSIA, so the fraction of oxidized DMS leading to SO_2 is significantly lowered. The concentration of $DMSO_2$, a terminal product of OH-initiated oxidation of DMS, remains low in the absence of heterogeneous reactions. These simulations suggest that

MSA may be the dominant oxidation product of DMS oxidation for conditions found in the high-latitude marine atmosphere with low temperatures.

The agreement between the present chamber study, our model, and ambient observations over a wide temperature range is consistent with OH-initiated DMS oxidation governing the formation of gas-phase MSA and H_2SO_4 in the remote atmosphere. Our observation of many intermediate products closes gaps between the measured and modeled MSA. Specifically, MSIA and HPMTF are useful intermediates that serve as markers for OH addition and hydrogen abstraction channels, respectively. Therefore, measurement and proper calibration of these two species become important in future laboratory experiments and field observations for studying DMS. These findings improve our understanding of the atmospheric DMS oxidation process and its contribution to the natural sulfur cycle and potentially the formation of biogenic aerosol and thus CCN.

■ ASSOCIATED CONTENT

Ⓢ Supporting Information

The Supporting Information is available free of charge at https://pubs.acs.org/doi/10.1021/acs.est.2c05154.

> Additional description of quantitative measurement of DMS and its oxidation products; quantum chemical calculation method; detailed chemistry mechanism used in the box model; HO_2 and OH estimation from the box model; heterogeneous wall reactions of DMS and O_3 in the CLOUD chamber; temperature effect on the DMS oxidation process; and reactions of DMS oxidation chemistry (PDF)

■ AUTHOR INFORMATION

Corresponding Author

Federico Bianchi − *Institute for Atmospheric and Earth System Research/Physics, Faculty of Science, University of Helsinki, 00014 Helsinki, Finland;* ⓘ orcid.org/0000-0003-2996-3604; Email: federico.bianchi@helsinki.fi

Authors

Jiali Shen − *Institute for Atmospheric and Earth System Research/Physics, Faculty of Science, University of Helsinki, 00014 Helsinki, Finland;* ⓘ orcid.org/0000-0001-8701-7929

Wiebke Scholz − *Institute of Ion Physics and Applied Physics, University of Innsbruck, 6020 Innsbruck, Austria*

Xu-Cheng He − *Institute for Atmospheric and Earth System Research/Physics, Faculty of Science, University of Helsinki, 00014 Helsinki, Finland;* ⓘ orcid.org/0000-0002-7416-306X

Putian Zhou − *Institute for Atmospheric and Earth System Research/Physics, Faculty of Science, University of Helsinki, 00014 Helsinki, Finland*

Guillaume Marie − *Institute for Atmospheric and Environmental Sciences, Goethe University Frankfurt, 60438 Frankfurt am Main, Germany;* Present Address: Division of Chemistry and Chemical Engineering, California Institute of Technology, Pasadena, CA 91125, USA

Mingyi Wang − *Center for Atmospheric Particle Studies, Carnegie Mellon University, Pittsburgh, Pennsylvania 15213, United States*

Ruby Marten − *Laboratory of Atmospheric Chemistry, Paul Scherrer Institute, CH-5232 Villigen, Switzerland*

Mihnea Surdu − *Laboratory of Atmospheric Chemistry, Paul Scherrer Institute, CH-5232 Villigen, Switzerland;* ⓘ orcid.org/0000-0003-1815-2750

Birte Rörup − *Institute for Atmospheric and Earth System Research/Physics, Faculty of Science, University of Helsinki, 00014 Helsinki, Finland*

Rima Baalbaki − *Institute for Atmospheric and Earth System Research/Physics, Faculty of Science, University of Helsinki, 00014 Helsinki, Finland*

Antonio Amorim − *CENTRA and Faculdade de Ciências da Universidade de Lisboa, 1749-016 Campo Grande, Lisboa, Portugal*

Farnoush Ataei − *Leibniz Institute for Tropospheric Research, 04318 Leipzig, Germany*

David M. Bell − *Laboratory of Atmospheric Chemistry, Paul Scherrer Institute, CH-5232 Villigen, Switzerland*

Barbara Bertozzi − *Institute of Meteorology and Climate Research, Karlsruhe Institute of Technology, 76344 Karlsruhe, Germany*

Zoé Brasseur − *Institute for Atmospheric and Earth System Research/Physics, Faculty of Science, University of Helsinki, 00014 Helsinki, Finland;* ⓘ orcid.org/0000-0001-5387-018X

Lucía Caudillo − *Institute for Atmospheric and Environmental Sciences, Goethe University Frankfurt, 60438 Frankfurt am Main, Germany*

Dexian Chen − *Center for Atmospheric Particle Studies, Carnegie Mellon University, Pittsburgh, Pennsylvania 15213, United States*

Biwu Chu − *Institute for Atmospheric and Earth System Research/Physics, Faculty of Science, University of Helsinki, 00014 Helsinki, Finland;* ⓘ orcid.org/0000-0002-7548-5669

Lubna Dada − *Laboratory of Atmospheric Chemistry, Paul Scherrer Institute, CH-5232 Villigen, Switzerland*

Jonathan Duplissy − *Institute for Atmospheric and Earth System Research/Physics, Faculty of Science, University of Helsinki, 00014 Helsinki, Finland; Helsinki Institute of Physics, University of Helsinki, 00014 Helsinki, Finland;* ⓘ orcid.org/0000-0001-8819-0264

Henning Finkenzeller − *Department of Chemistry and Cooperative Institute for Research in the Environmental Sciences, University of Colorado Boulder, Boulder, Colorado 80309, United States;* ⓘ orcid.org/0000-0002-8349-3714

Manuel Granzin − *Institute for Atmospheric and Environmental Sciences, Goethe University Frankfurt, 60438 Frankfurt am Main, Germany*

Roberto Guida − *CERN, the European Organization for Nuclear Research, CH-1211 Geneva 23, Switzerland*

Martin Heinritzi − *Institute for Atmospheric and Environmental Sciences, Goethe University Frankfurt, 60438 Frankfurt am Main, Germany*

Victoria Hofbauer − *Center for Atmospheric Particle Studies, Carnegie Mellon University, Pittsburgh, Pennsylvania 15213, United States*

Siddharth Iyer − *Aerosol Physics Laboratory, Physics Unit, Faculty of Engineering and Natural Sciences, Tampere University, 33014 Tampere, Finland*

Deniz Kemppainen − *Institute for Atmospheric and Earth System Research/Physics, Faculty of Science, University of Helsinki, 00014 Helsinki, Finland*

Weimeng Kong − *Division of Chemistry and Chemical Engineering, California Institute of Technology, Pasadena, California 91125, United States*

Jordan E. Krechmer − *Aerodyne Research, Inc., Billerica, Massachusetts 01821, United States*

Andreas Kürten − *Institute for Atmospheric and Environmental Sciences, Goethe University Frankfurt, 60438 Frankfurt am Main, Germany*

Houssni Lamkaddam − *Laboratory of Atmospheric Chemistry, Paul Scherrer Institute, CH-5232 Villigen, Switzerland*

Chuan Ping Lee − *Laboratory of Atmospheric Chemistry, Paul Scherrer Institute, CH-5232 Villigen, Switzerland*

Brandon Lopez − *Center for Atmospheric Particle Studies, Carnegie Mellon University, Pittsburgh, Pennsylvania 15213, United States*

Naser G. A. Mahfouz − *Atmospheric and Oceanic Sciences, Princeton University, Princeton, New Jersey 08540, United States*

Hanna E. Manninen − *CERN, the European Organization for Nuclear Research, CH-1211 Geneva 23, Switzerland*

Dario Massabò − *Department of Physics, University of Genoa & INFN, 16146 Genoa, Italy*

Roy L. Mauldin − *Department of Chemistry, Carnegie Mellon University, Pittsburgh, Pennsylvania 15213, United States; Department of Atmospheric and Oceanic Sciences, University of Colorado Boulder, Boulder, Colorado 80309, United States*

Bernhard Mentler − *Institute of Ion Physics and Applied Physics, University of Innsbruck, 6020 Innsbruck, Austria*

Tatjana Müller − *Institute for Atmospheric and Environmental Sciences, Goethe University Frankfurt, 60438 Frankfurt am Main, Germany*

Joschka Pfeifer − *CERN, the European Organization for Nuclear Research, CH-1211 Geneva 23, Switzerland*

Maxim Philippov − *P.N. Lebedev Physical Institute of the Russian Academy of Sciences, 119991 Moscow, Russia;* ⊙ orcid.org/0000-0003-4302-0020

Ana A. Piedehierro − *Finnish Meteorological Institute, 00560 Helsinki, Finland;* ⊙ orcid.org/0000-0002-1900-8139

Pontus Roldin − *Division of Nuclear Physics, Lund University, 22100 Lund, Sweden*

Siegfried Schobesberger − *Department of Applied Physics, University of Eastern Finland, 70211 Kuopio, Finland*

Mario Simon − *Institute for Atmospheric and Environmental Sciences, Goethe University Frankfurt, 60438 Frankfurt am Main, Germany*

Dominik Stolzenburg − *Institute for Atmospheric and Earth System Research/Physics, Faculty of Science, University of Helsinki, 00014 Helsinki, Finland*

Yee Jun Tham − *School of Marine Sciences, Sun Yat-sen University, 519082 Zhuhai, China; Institute for Atmospheric and Earth System Research/Physics, Faculty of Science, University of Helsinki, 00014 Helsinki, Finland*

António Tomé − *Institute Infante Dom Luíz, University of Beira Interior, 6200-001 Covilhã, Portugal*

Nsikanabasi Silas Umo − *Institute of Meteorology and Climate Research, Karlsruhe Institute of Technology, 76344 Karlsruhe, Germany*

Dongyu Wang − *Laboratory of Atmospheric Chemistry, Paul Scherrer Institute, CH-5232 Villigen, Switzerland*

Yonghong Wang − *Institute for Atmospheric and Earth System Research/Physics, Faculty of Science, University of Helsinki, 00014 Helsinki, Finland;* ⊙ orcid.org/0000-0003-2498-9143

Stefan K. Weber − *CERN, the European Organization for Nuclear Research, CH-1211 Geneva 23, Switzerland; Institute for Atmospheric and Environmental Sciences, Goethe University Frankfurt, 60438 Frankfurt am Main, Germany*

André Welti − *Finnish Meteorological Institute, 00560 Helsinki, Finland*

Robin Wollesen de Jonge − *Division of Nuclear Physics, Lund University, 22100 Lund, Sweden*

Yusheng Wu − *Institute for Atmospheric and Earth System Research/Physics, Faculty of Science, University of Helsinki, 00014 Helsinki, Finland*

Marcel Zauner-Wieczorek − *Institute for Atmospheric and Environmental Sciences, Goethe University Frankfurt, 60438 Frankfurt am Main, Germany*

Felix Zust − *Institute of Ion Physics and Applied Physics, University of Innsbruck, 6020 Innsbruck, Austria*

Urs Baltensperger − *Laboratory of Atmospheric Chemistry, Paul Scherrer Institute, CH-5232 Villigen, Switzerland*

Joachim Curtius − *Institute for Atmospheric and Environmental Sciences, Goethe University Frankfurt, 60438 Frankfurt am Main, Germany*

Richard C. Flagan − *Division of Chemistry and Chemical Engineering, California Institute of Technology, Pasadena, California 91125, United States*

Armin Hansel − *Institute of Ion Physics and Applied Physics, University of Innsbruck, 6020 Innsbruck, Austria;* ⊙ orcid.org/0000-0002-1062-2394

Ottmar Möhler − *Institute of Meteorology and Climate Research, Karlsruhe Institute of Technology, 76344 Karlsruhe, Germany*

Tuukka Petäjä − *Institute for Atmospheric and Earth System Research/Physics, Faculty of Science, University of Helsinki, 00014 Helsinki, Finland*

Rainer Volkamer − *Department of Chemistry and Cooperative Institute for Research in the Environmental Sciences, University of Colorado Boulder, Boulder, Colorado 80309, United States;* ⊙ orcid.org/0000-0002-0899-1369

Markku Kulmala − *Institute for Atmospheric and Earth System Research/Physics, Faculty of Science, University of Helsinki, 00014 Helsinki, Finland; Helsinki Institute of Physics, University of Helsinki, 00014 Helsinki, Finland; Joint International Research Laboratory of Atmospheric and Earth System Sciences, School of Atmospheric Sciences, Nanjing University, 210023 Nanjing, China; Aerosol and Haze Laboratory, Beijing Advanced Innovation Center for Soft Matter Science and Engineering, Beijing University of Chemical Technology, 100029 Beijing, China*

Katrianne Lehtipalo − *Institute for Atmospheric and Earth System Research/Physics, Faculty of Science, University of Helsinki, 00014 Helsinki, Finland; Finnish Meteorological Institute, 00560 Helsinki, Finland*

Matti Rissanen − *Aerosol Physics Laboratory, Physics Unit, Faculty of Engineering and Natural Sciences, Tampere University, 33014 Tampere, Finland;* ⊙ orcid.org/0000-0003-0463-8098

Jasper Kirkby − *CERN, the European Organization for Nuclear Research, CH-1211 Geneva 23, Switzerland; Institute for Atmospheric and Environmental Sciences, Goethe University Frankfurt, 60438 Frankfurt am Main, Germany*

Imad El-Haddad − *Laboratory of Atmospheric Chemistry, Paul Scherrer Institute, CH-5232 Villigen, Switzerland;* orcid.org/0000-0002-2461-7238

Mikko Sipilä − *Institute for Atmospheric and Earth System Research/Physics, Faculty of Science, University of Helsinki, 00014 Helsinki, Finland*

Neil M. Donahue − *Center for Atmospheric Particle Studies, Carnegie Mellon University, Pittsburgh, Pennsylvania 15213, United States; Department of Chemistry, Department of Chemical Engineering, and Department of Engineering and Public Policy, Carnegie Mellon University, Pittsburgh, Pennsylvania 15213, United States;* orcid.org/0000-0003-3054-2364

Douglas R. Worsnop − *Institute for Atmospheric and Earth System Research/Physics, Faculty of Science, University of Helsinki, 00014 Helsinki, Finland; Aerodyne Research, Inc., Billerica, Massachusetts 01821, United States*

Complete contact information is available at:
https://pubs.acs.org/10.1021/acs.est.2c05154

Author Contributions

J.S., X.-C.H., and M.Sip. planned the experiments. J.S., W.S., X.-C.H., G.M., M.W., R.M., B.R., R.B., L.C., F.A., D.M.B., B.B., Z.B., D.C., B.C., L.D., J.D., H.F., M.G., R.G., M.H., V.H., W.K., J.E.K., A.K., H.L., C.P.L., B.L., N.G.A.M., H.E.M., D.M., R.L.M., B.M., T.M., T.P., J.P., M.P., A.A.P., S.S., M.Si., M.Su., Y.J.T., A.T., N.S.U., D.W., Y.Wang., S.K.W., A.W., Y.Wu., M.Z.-W., U.B., J.C., R.C.F., R.V., O.M., K.M., K.L., M.R., J.K., I.E.-H., F.B., and M.Sip. prepared the CLOUD facility or measuring instruments. J.S., W.S., X.-C.H., G.M., M.W., R.M., B.R., R.B., L.C., A.A., F.A., D.M.B., B.B., D.C., J.D., H.F., M.G., M.H., V.H., D.K., W.K., J.E.K., H.L., C.P.L., B.L., N.G.A.M., D.M., R.L.M., B.M., T.M., J.P., M.Sim., M.Su., Y.J.T., A.T., D.W., S.K.W., Y.Wu., M.Z.-W., J.C., R.C.F., R.V., and J.K. collected the data. J.S., W.S., X.-C.H., P.Z., G.M., M.W., R.M., B.R., L.C., S.I., J.K., M.Sim., M.Su., and S.K.W. analyzed the data. J.S., W.S., X.-C.H., P.Z., S.I., P.R., M.Sim., D.S., R.W.D.J., U.B., J.C., R.C.F., A.H., K.M., K.L., M.R., J.K., I.E.-H., F.B., M.Sip., N.M.D., and D.R.W. contributed to the scientific discussion. J.S. and N.M.D. wrote the manuscript with contributions from W.S., X.-C.H., M.R., J.K., I.E.-H., F.B., and D.R.W. J.S., W.S., X.-C.H., P.Z., R.B., Z.B., J.D., H.F., N.G.A.M., R.G., P.R., R.W.D.J., S.S., D.S., D.W., M.Z.-W., U.B., M.R., J.K., I.E.-H., F.B., M.S., N.M.D., and D.R.W. commented on and edited the manuscript.

Funding

Notes

The authors declare no competing financial interest.

REFERENCES

(1) Stefels, J.; Steinke, M.; Turner, S.; Malin, G.; Belviso, S. Environmental Constraints on the Production and Removal of the Climatically Active Gas Dimethylsulphide (DMS) and Implications for Ecosystem Modelling. *Biogeochemistry* **2007**, *83*, 245−275.

(2) Carpenter, L. J.; Archer, S. D.; Beale, R. Ocean-Atmosphere Trace Gas Exchange. *Chem. Soc. Rev.* **2012**, *41*, 6473−6506.

(3) Bates, T.; Lamb, B.; Guenther, A.; Dignon, J.; Stoiber, R. Sulfur Emissions to the Atmosphere from Natural Sources. *J. Atmos. Chem.* **1992**, *14*, 315−337.

(4) Carslaw, K. S.; Boucher, O.; Spracklen, D. V.; Mann, G. W.; Rae, J. G. L.; Woodward, S.; Kulmala, M. A review of natural aerosol interactions and feedbacks within the Earth system. *Atmos. Chem. Phys.* **2010**, *10*, 1701−1737.

(5) Charlson, R. J.; Lovelock, J. E.; Andreae, M. O.; Warren, S. G. Oceanic phytoplankton, atmospheric sulphur, cloud albedo and climate. *Nature* **1987**, *326*, 655−661.

(6) Bates, T. S.; Calhoun, J. A.; Quinn, P. K. Variations in the methanesulfonate to sulfate molar ratio in submicrometer marine aerosol particles over the south Pacific Ocean. *J. Geophys. Res.: Atmos.* **1992**, *97*, 9859−9865.

(7) Ayers, G. P.; Cainey, J. M.; Granek, H.; Leck, C. Dimethylsulfide oxidation and the ratio of methanesulfonate to non sea-salt sulfate in the marine aerosol. *J. Atmos. Chem.* **1996**, *25*, 307−325.

(8) Covert, D. S.; Kapustin, V. N.; Quinn, P. K.; Bates, T. S. New particle formation in the marine boundary layer. *J. Geophys. Res.: Atmos.* **1992**, *97*, 20581−20589.

(9) Kreidenweis, S. M.; Seinfeld, J. H. Nucleation of sulfuric acid-water and methanesulfonic acid-water solution particles: implications for the atmospheric chemistry of organosulfur species. *Atmos. Environ* **1988**, *22*, 283−296.

(10) McMurry, P. H.; Fink, M.; Sakurai, H.; Stolzenburg, M.; Mauldin, R., III; Smith, J.; Eisele, F.; Moore, K.; Sjostedt, S.; Tanner, D.; et al. A criterion for new particle formation in the sulfur-rich Atlanta atmosphere. *J. Geophys. Res.: Atmos.* **2005**, *110*, 1−10.

(11) Dawson, M. L.; Varner, M. E.; Perraud, V.; Ezell, M. J.; Gerber, R. B.; Finlayson-Pitts, B. J. Simplified mechanism for new particle formation from methanesulfonic acid, amines, and water via experiments and ab initio calculations. *Proc. Natl. Acad. Sci. U.S.A.* **2012**, *109*, 18719−18724.

(12) Beck, L. J.; Sarnela, N.; Junninen, H.; Hoppe, C. J. M.; Garmash, O.; Bianchi, F.; Riva, M.; Rose, C.; Peräkylä, O.; Wimmer, D.; Kausiala, O.; Jokinen, T.; Ahonen, L.; Mikkilä, J.; Hakala, J.; He, X. C.; Kontkanen, J.; Wolf, K. K. E.; Cappelletti, D.; Mazzola, M.; Traversi, R.; Petroselli, C.; Viola, A. P.; Vitale, V.; Lange, R.; Massling, A.; Nøjgaard, J. K.; Krejci, R.; Karlsson, L.; Zieger, P.; Jang, S.; Lee, K.; Vakkari, V.; Lampilahti, J.; Thakur, R. C.; Leino, K.; Kangasluoma, J.; Duplissy, E. M.; Siivola, E.; Marbouti, M.; Tham, Y. J.; Saiz-Lopez, A.; Petäjä, T.; Ehn, M.; Worsnop, D. R.; Skov, H.; Kulmala, M.; Kerminen, V. M.; Sipilä, M. Differing mechanisms of new particle formation at two Arctic sites. *Geophys. Res. Lett.* **2021**, *48*, No. e2020GL091334.

(13) Kirkby, J.; Curtius, J.; Almeida, J.; Dunne, E.; Duplissy, J.; Ehrhart, S.; Franchin, A.; Gagne, S.; Ickes, L.; Kurten, A.; Kupc, A.; Metzger, A.; Riccobono, F.; Rondo, L.; Schobesberger, S.; Tsagkogeorgas, G.; Wimmer, D.; Amorim, A.; Bianchi, F.; Breitenlechner, M.; David, A.; Dommen, J.; Downard, A.; Ehn, M.; Flagan, R. C.; Haider, S.; Hansel, A.; Hauser, D.; Jud, W.; Junninen, H.; Kreissl, F.; Kvashin, A.; Laaksonen, A.; Lehtipalo, K.; Lima, J.; Lovejoy, E. R.; Makhmutov, V.; Mathot, S.; Mikkila, J.; Minginette, P.; Mogo, S.; Nieminen, T.; Onnela, A.; Pereira, P.; Petaja, T.; Schnitzhofer, R.; Seinfeld, J. H.; Sipila, M.; Stozhkov, Y.; Stratmann, F.; Tome, A.; Vanhanen, J.; Viisanen, Y.; Vrtala, A.; Wagner, P. E.; Walther, H.; Weingartner, E.; Wex, H.; Winkler, P. M.; Carslaw, K. S.; Worsnop, D. R.; Baltensperger, U.; Kulmala, M. Role of sulphuric acid, ammonia and galactic cosmic rays in atmospheric aerosol nucleation. *Nature* **2011**, *476*, 429−U77.

(14) Bolin, B.; Charlson, J. On the role of the tropospheric sulfur cycle in the shortwave radioactive climate of the earth. *Ambio* **1976**, *5*, 47−54.

(15) Quinn, P. K.; Bates, T. S. The case against climate regulation via oceanic phytoplankton sulphur emissions. *Nature* **2011**, *480*, 51−56.

(16) Carslaw, K. S.; Lee, L. A.; Reddington, C. L.; Pringle, K. J.; Rap, A.; Forster, P. M.; Mann, G. W.; Spracklen, D. V.; Woodhouse, M. T.; Regayre, L. A.; Pierce, J. R. Large contribution of natural aerosols to uncertainty in indirect forcing. *Nature* **2013**, *503*, 67−71.

(17) Chen, L.; Wang, J.; Gao, Y.; Xu, G.; Yang, X.; Lin, Q.; Zhang, Y. Latitudinal distributions of atmospheric MSA and MSA/nss-SO_4^{2-} ratios in summer over the high latitude regions of the Southern and Northern Hemispheres. *J. Geophys. Res.: Atmos.* **2012**, *117*, No. 306.

(18) Ayers, G. P.; Ivey, J. P.; Gillett, R. W. Coherence between seasonal cycles of dimethyl sulphide, methanesulphonate and sulphate in marine air. *Nature* **1991**, *349*, 404−406.

(19) Mauldin, R. L., III; Tanner, D. J.; Heath, J. A.; Huebert, B. J.; Eisele, F. L. Observations of H_2SO_4 and MSA during PEM-Tropics-A. *J. Geophys. Res.: Atmos.* **1999**, *104*, 5801−5816.

(20) Mauldin, R. L., III; Eisele, F. L.; Tanner, D. J.; Kosciuch, E.; Shetter, R.; Lefer, B.; Hall, S. R.; Nowak, J. B.; Buhr, M.; Chen, G.; Wang, P.; Davis, D. Measurements of OH, H_2SO_4, and MSA at the South Pole during ISCAT. *Geophys. Res. Lett.* **2001**, *28*, 3629−3632.

(21) Berresheim, H.; Elste, T.; Tremmel, H. G.; Allen, A. G.; Hansson, H.-C.; Rosman, K.; Dal Maso, M.; Mäkelä, J. M.; Kulmala, M.; O'Dowd, C. D. Gas-aerosol relationships of H_2SO_4, MSA, and OH: Observations in the coastal marine boundary layer at Mace Head, Ireland. *J. Geophys. Res.: Atmos.* **2002**, *107*, PAR5-1−PAR 5-12.

(22) Bardouki, H.; Berresheim, H.; Vrekoussis, M.; Sciare, J.; Kouvarakis, G.; Oikonomou, K.; Schneider, J.; Mihalopoulos, N. Gaseous (DMS, MSA, SO_2, H_2SO_4 and DMSO) and particulate (sulfate and methanesulfonate) sulfur species over the northeastern coast of Crete. *Atmos. Chem. Phys.* **2003**, *3*, 1871−1886.

(23) Baccarini, A.; Dommen, J.; Lehtipalo, K.; Henning, S.; Modini, R. L.; Gysel-Beer, M.; Baltensperger, U.; Schmale, J. Low-volatility vapors and new particle formation over the Southern Ocean during the Antarctic Circumnavigation Expedition. *J. Geophys. Res.: Atmos.* **2021**, *126*, No. e2021JD035126.

(24) O'Dowd, C. D.; Jimenez, J. L.; Bahreini, R.; Flagan, R. C.; Seinfeld, J. H.; Hämeri, K.; Pirjola, L.; Kulmala, M.; Jennings, S. G.; Hoffmann, T. Marine aerosol formation from biogenic iodine emissions. *Nature* **2002**, *417*, 632−636.

(25) He, X.-C.; Tham, Y. J.; Dada, L.; Wang, M.; Finkenzeller, H.; Stolzenburg, D.; Iyer, S.; Simon, M.; Kürten, A.; Shen, J.; Rörup, B.; Rissanen, M.; Schobesberger, S.; Baalbaki, R.; Wang, D. S.; Koenig, T. K.; Jokinen, T.; Sarnela, N.; Beck, L. J.; Almeida, J.; Amanatidis, S.; Amorim, A.; Ataei, F.; Baccarini, A.; Bertozzi, B.; Bianchi, F.; Brilke, S.; Caudillo, L.; Chen, D.; Chiu, R.; Chu, B.; Dias, A.; Ding, A.; Dommen, J.; Duplissy, J.; Haddad, I. E.; Carracedo, L. G.; Granzin, M.; Hansel, A.; Heinritzi, M.; Hofbauer, V.; Junninen, H.; Kangasluoma, J.; Kemppainen, D.; Kim, C.; Kong, W.; Krechmer, J. E.; Kvashin, A.; Laitinen, T.; Lamkaddam, H.; Lee, C. P.; Lehtipalo, K.; Leiminger, M.; Li, Z.; Makhmutov, V.; Manninen, H. E.; Marie, G.; Marten, R.; Mathot, S.; Mauldin, R. L.; Mentler, B.; Möhler, O.; Müller, T.; Nie, W.; Onnela, A.; Petäjä, T.; Pfeifer, J.; Philippov, M.; Ranjithkumar, A.; Saiz-Lopez, A.; Salma, I.; Scholz, W.; Schuchmann, S.; Schulze, B.; Steiner, G.; Stozhkov, Y.; Tauber, C.; Tomé, A.; Thakur, R. C.; Väisänen, O.; Vazquez-Pufleau, M.; Wagner, A. C.; Wang, Y.; Weber, S. K.; Winkler, P. M.; Wu, Y.; Xiao, M.; Yan, C.; Ye, Q.; Ylisirniö, A.; Zauner-Wieczorek, M.; Zha, Q.; Zhou, P.; Flagan, R. C.; Curtius, J.; Baltensperger, U.; Kulmala, M.; Kerminen, V.-M.; Kurtén, T.; Donahue, N. M.; Volkamer, R.; Kirkby, J.; Worsnop, D. R.; Sipilä, M. Role of iodine oxoacids in atmospheric aerosol nucleation. *Science* **2021**, *371*, 589−595.

(26) Arsene, C.; Barnes, I.; Becker, K. H.; Mocanu, R. FT-IR product study on the photo-oxidation of dimethyl sulphide in the presence of NO_x—temperature dependence. *Atmos. Environ.* **2001**, *35*, 3769−3780.

(27) Berndt, T.; Richters, S. Products of the reaction of OH radicals with dimethyl sulphide in the absence of NO_x: Experiment and simulation. *Atmos. Environ.* **2012**, *47*, 316−322.

(28) Bardouki, H.; da Rosa, M. B.; Mihalopoulos, N.; Palm, W. U.; Zetzsch, C. Kinetics and mechanism of the oxidation of dimethylsulfoxide (DMSO) and methanesulfinate (MSI⁻) by OH radicals in aqueous medium. *Atmos. Environ.* **2002**, *36*, 4627−4634.

(29) Berndt, T.; Scholz, W.; Mentler, B.; Fischer, L.; Hoffmann, E. H.; Tilgner, A.; Hyttinen, N.; Prisle, N. L.; Hansel, A.; Herrmann, H. Fast Peroxy Radical Isomerization and OH Recycling in the Reaction of OH Radicals with Dimethyl Sulfide. *J. Phys. Chem. Lett.* **2019**, *10*, 6478−6483.

(30) Ye, Q.; Goss, M. B.; Isaacman-VanWertz, G.; Zaytsev, A.; Massoli, P.; Lim, C.; Croteau, P.; Canagaratna, M.; Knopf, D. A.; Keutsch, F. N.; Heald, C. L.; Kroll, J. H. Organic Sulfur Products and Peroxy Radical Isomerization in the OH Oxidation of Dimethyl Sulfide. *ACS Earth Space Chem.* **2021**, *5*, 2013−2020.

(31) Wu, R.; Wang, S.; Wang, L. New Mechanism for the Atmospheric Oxidation of Dimethyl Sulfide. The Importance of Intramolecular Hydrogen Shift in a CH_3SCH_2OO Radical. *J. Phys. Chem. A* **2015**, *119*, 112−117.

(32) Veres, P. R.; Neuman, J. A.; Bertram, T. H.; Assaf, E.; Wolfe, G. M.; Williamson, C. J.; Weinzierl, B.; Tilmes, S.; Thompson, C. R.; Thames, A. B.; Schroder, J. C.; Saiz-Lopez, A.; Rollins, A. W.; Roberts, J. M.; Price, D.; Peischl, J.; Nault, B. A.; Møller, K. H.; Miller, D. O.; Meinardi, S.; Li, Q.; Lamarque, J.-F.; Kupc, A.; Kjaergaard, H. G.; Kinnison, D.; Jimenez, J. L.; Jernigan, C. M.; Hornbrook, R. S.; Hills, A.; Dollner, M.; Day, D. A.; Cuevas, C. A.; Campuzano-Jost, P.; Burkholder, J.; Bui, T. P.; Brune, W. H.; Brown, S. S.; Brock, C. A.; Bourgeois, I.; Blake, D. R.; Apel, E. C.; Ryerson, T. B. Global airborne sampling reveals a previously unobserved dimethyl sulfide oxidation mechanism in the marine atmosphere. *Proc. Natl. Acad. Sci. U.S.A.* **2020**, *117*, 4505−4510.

(33) Barnes, I.; Bastian, V.; Becker, K. H. Kinetics and mechanisms of the reaction of OH radicals with dimethyl sulfide. *Int. J. Chem. Kinet.* **1988**, *20*, 415−431.

(34) Barone, S. B.; Turnipseed, A. A.; Ravishankara, A. R. Reaction of OH with Dimethyl Sulfide (DMS). 1. Equilibrium Constant for OH + DMS Reaction and the Kinetics of the OH·DMS + O_2 Reaction. *J. Phys. Chem. A* **1996**, *100*, 14694−14702.

(35) Barnes, I.; Hjorth, J.; Mihalopoulos, N. Dimethyl Sulfide and Dimethyl Sulfoxide and Their Oxidation in the Atmosphere. *Chem. Rev.* **2006**, *106*, 940−975.34.

(36) Butkovskaya, N. I.; Poulet, G.; LeBras, G. Discharge Flow Study of the Reactions of Chlorine and Fluorine Atoms with Dimethyl Sulfide. *J. Phys. Chem. A* **1995**, *99*, 4536−4543.

(37) Chen, Q.; Sherwen, T.; Evans, M.; Alexander, B. DMS oxidation and sulfur aerosol formation in the marine troposphere: a focus on reactive halogen and multiphase chemistry. *Atmos. Chem. Phys.* **2018**, *18*, 13617−13637.

(38) Von Glasow, R.; Crutzen, P. J. Model study of multiphase DMS oxidation with a focus on halogens. *Atmos. Chem. Phys.* **2004**, *4*, 589−608.

(39) Barnes, I.; Bastian, V.; Becker, K. H.; Overath, R. D. Kinetic studies of the reactions of IO, BrO, and ClO with dimethylsulfide. *Int. J. Chem. Kinet.* **1991**, *23*, 579−591.

(40) Hoffmann, E. H.; Tilgner, A.; Schrödner, R.; Bräuer, P.; Wolke, R.; Herrmann, H. An advanced modeling study on the impacts and atmospheric implications of multiphase dimethyl sulfide chemistry. *Proc. Natl. Acad. Sci. U.S.A.* **2016**, *113*, 11776−11781.

(41) Wollesen de Jonge, R.; Elm, J.; Rosati, B.; Christiansen, S.; Hyttinen, N.; Lüdemann, D.; Bilde, M.; Roldin, P. Secondary aerosol formation from dimethyl sulfide—improved mechanistic understanding based on smog chamber experiments and modelling. *Atmos. Chem. Phys.* **2021**, *21*, 9955−9976.

(42) Werle, P.; Slemr, F.; Maurer, K.; Kormann, R.; Mücke, R.; Jänker, B. Near- and mid-infrared laser-optical sensors for gas analysis. *Opt. Lasers Eng.* **2002**, *37*, 101−114.

(43) Breitenlechner, M.; Fischer, L.; Hainer, M.; Heinritzi, M.; Curtius, J.; Hansel, A. PTR3: An Instrument for Studying the Lifecycle of Reactive Organic Carbon in the Atmosphere. *Anal. Chem.* **2017**, *89*, 5824−5831.

(44) Canaval, E.; Hyttinen, N.; Schmidbauer, B.; Fischer, L.; Hansel, A. NH4+ Association and Proton Transfer Reactions With a Series of Organic Molecules. *Front. Chem.* **2019**, *7*, No. 191.

(45) Jokinen, T.; Sipilä, M.; Junninen, H.; Ehn, M.; Lönn, G.; Hakala, J.; Petäjä, T.; Mauldin Iii, R. L.; Kulmala, M.; Worsnop, D. R. Atmospheric sulphuric acid and neutral cluster measurements using CI-APi-TOF. *Atmos. Chem. Phys.* **2012**, *12*, 4117−4125.

(46) Kürten, A.; Rondo, L.; Ehrhart, S.; Curtius, J. Performance of a corona ion source for measurement of sulfuric acid by chemical ionization mass spectrometry. *Atmos. Meas. Tech.* **2011**, *4*, 437−443.

(47) Kürten, A.; Rondo, L.; Ehrhart, S.; Curtius, J. Calibration of a Chemical Ionization Mass Spectrometer for the Measurement of Gaseous Sulfuric Acid. *J. Phys. Chem. A* **2012**, *116*, 6375−6386.

(48) Hansel, A.; Scholz, W.; Mentler, B.; Fischer, L.; Berndt, T. Detection of RO$_2$ radicals and other products from cyclohexene ozonolysis with NH$_4^+$ and acetate chemical ionization mass spectrometry. *Atmos. Environ.* **2018**, *186*, 248−255.

(49) Lopez-Hilfiker, F. D.; Mohr, C.; Ehn, M.; Rubach, F.; Kleist, E.; Wildt, J.; Mentel, T. F.; Lutz, A.; Hallquist, M.; Worsnop, D.; Thornton, J. A. A novel method for online analysis of gas and particle composition: description and evaluation of a Filter Inlet for Gases and AEROsols (FIGAERO). *Atmos. Meas. Tech.* **2014**, *7*, 983−1001.

(50) Rissanen, M. P.; Mikkilä, J.; Iyer, S.; Hakala, J. Multi-scheme chemical ionization inlet (MION) for fast switching of reagent ion chemistry in atmospheric pressure chemical ionization mass spectrometry (CIMS) applications. *Atmos. Meas. Tech.* **2019**, *12*, 6635−6646.

(51) Damian, V.; Sandu, A.; Damian, M.; Potra, F.; Carmichael, G. R. The kinetic preprocessor KPP-a software environment for solving chemical kinetics. *Comput. Chem. Eng.* **2002**, *26*, 1567−1579.

(52) Sandu, A.; Verwer, J. G.; Blom, J. G.; Spee, E. J.; Carmichael, G. R.; Potra, F. A. Benchmarking stiff ode solvers for atmospheric chemistry problems II: Rosenbrock solvers. *Atmos. Environ.* **1997**, *31*, 3459−3472.

(53) Sørensen, S.; Falbe-Hansen, H.; Mangoni, M.; Hjorth, J.; Jensen, N. R. Observation of DMSO and CH$_3$S(O)OH from the gas phase reaction between DMS and OH. *J. Atmos. Chem.* **1996**, *24*, 299−315.

(54) Kukui, A.; Borissenko, D.; Laverdet, G.; Le Bras, G. Gas-Phase Reactions of OH Radicals with Dimethyl Sulfoxide and Methane Sulfinic Acid Using Turbulent Flow Reactor and Chemical Ionization Mass Spectrometry. *J. Phys. Chem. B* **2003**, *107*, 5732−5742.

(55) Lv, G.; Zhang, C.; Sun, X. Understanding the oxidation mechanism of methanesulfinic acid by ozone in the atmosphere. *Sci. Rep.* **2019**, *9*, No. 322.

(56) Donahue, N. M. Reaction Barriers: Origin and Evolution. *Chem. Rev.* **2003**, *103*, 4593−4604.

(57) Yin, F.; Grosjean, D.; Seinfeld, J. H. J. J. o. A. C. Photooxidation of dimethyl sulfide and dimethyl disulfide. I: Mechanism development. *J. Atmos. Chem.* **1990**, *11*, 309−364.

(58) Lucas, D. D.; Prinn, R. G. Mechanistic studies of dimethylsulfide oxidation products using an observationally constrained model. *J. Geophys. Res.: Atmos.* **2002**, *107*, No. ACH-12.

(59) Saunders, S. M.; Jenkin, M. E.; Derwent, R. G.; Pilling, M. J. Protocol for the development of the Master Chemical Mechanism, MCM v3 (Part A): tropospheric degradation of non-aromatic volatile organic compounds. *Atmos. Chem. Phys.* **2003**, *3*, 161−180.

(60) Turnipseed, A. A.; Barone, S. B.; Ravishankara, A. R. Reactions of methylthio and (methylthio)dioxy with ozone, nitrogen dioxide, and nitric oxide. *J. Phys. Chem. C* **1993**, *97*, 5926−5934.

(61) Campolongo, F.; Saltelli, A.; Jensen, N. R.; Wilson, J.; Hjorth, J. The Role of Multiphase Chemistry in the Oxidation of Dimethylsulphide (DMS). A Latitude Dependent Analysis. *J. Atmos. Chem.* **1999**, *32*, 327−356.

(62) Patroescu, I. V.; Barnes, I.; Becker, K. H.; Mihalopoulos, N. FT-IR product study of the OH-initiated oxidation of DMS in the presence of NO$_x$. *Atmos. Environ.* **1998**, *33*, 25−35.

(63) Hoffmann, E. H.; Schrödner, R.; Tilgner, A.; Wolke, R.; Herrmann, H. CAPRAM reduction towards an operational multiphase halogen and dimethyl sulfide chemistry treatment in the chemistry transport model COSMO-MUSCAT(5.04e). *Geosci. Model Dev.* **2020**, *13*, 2587−2609.

(64) Edtbauer, A.; Stönner, C.; Pfannerstill, E. Y.; Berasategui, M.; Walter, D.; Crowley, J. N.; Lelieveld, J.; Williams, J. A new marine biogenic emission: methane sulfonamide (MSAM), dimethyl sulfide (DMS), and dimethyl sulfone (DMSO$_2$) measured in air over the Arabian Sea. *Atmos. Chem. Phys.* **2020**, *20*, 6081−6094.

(65) Nowak, J. B.; Davis, D. D.; Chen, G.; Eisele, F. L.; Mauldin, R. L.; Tanner, D. J.; Cantrell, C.; Kosciuch, E.; Bandy, A.; Thornton, D.; Clarke, A. Airborne observations of DMSO, DMS, and OH at marine tropical latitudes. *Geophys. Res. Lett.* **2001**, *28*, 2201−2204.

(66) Khan, M. A. H.; Bannan, T. J.; Holland, R.; Shallcross, D. E.; Archibald, A. T.; Matthews, E.; Back, A.; Allan, J.; Coe, H.; Artaxo, P.; Percival, C. J. Impacts of Hydroperoxymethyl Thioformate on the Global Marine Sulfur Budget. *ACS Earth Space Chem.* **2021**, *5*, 2577−2586.

(67) Novak, G. A.; Fite, C. H.; Holmes, C. D.; Veres, P. R.; Neuman, J. A.; Faloona, I.; Thornton, J. A.; Wolfe, G. M.; Vermeuel, M. P.; Jernigan, C. M.; Peischl, J.; Ryerson, T. B.; Thompson, C. R.; Bourgeois, I.; Warneke, C.; Gkatzelis, G. I.; Coggon, M. M.; Sekimoto, K.; Bui, T. P.; Dean-Day, J.; Diskin, G. S.; DiGangi, J. P.; Nowak, J. B.; Moore, R. H.; Wiggins, E. B.; Winstead, E. L.; Robinson, C.; Thornhill, K. L.; Sanchez, K. J.; Hall, S. R.; Ullmann, K.; Dollner, M.; Weinzierl, B.; Blake, D. R.; Bertram, T. H. Rapid cloud removal of dimethyl sulfide oxidation products limits SO$_2$ and cloud condensation nuclei production in the marine atmosphere. *Proc. Natl. Acad. Sci. U.S.A.* **2021**, *118*, No. e2110472118.

(68) Jokinen, T.; Sipilä, M.; Kontkanen, J.; Vakkari, V.; Tisler, P.; Duplissy, E.-M.; Junninen, H.; Kangasluoma, J.; Manninen, H. E.; Petäjä, T.; Kulmala, M.; Worsnop, D. R.; Kirkby, J.; Virkkula, A.; Kerminen, V.-M. Ion-induced sulfuric acid-ammonia nucleation drives particle formation in coastal Antarctica. *Sci. Adv.* **2018**, *4*, No. eaat9744.